Enabling process science with CubeSat intersections: An orbit resampling study inspired by PREFIRE

Natasha Vos[1], Tristan S. L'Ecuyer[1,2], Tim Michaels[3]

5   [1]Department of Atmospheric and Oceanic Sciences, University of Wisconsin-Madison, Madison, WI, USA
[2]Cooperative Institute for Meteorological Satellite Studies, University of Wisconsin-Madison, Madison, WI, USA
[3]Space Science and Engineering Center, University of Wisconsin-Madison, Madison, WI, USA

Correspondence to: Natasha Vos (midwesternmeteorologist@gmail.com)

Abstract. The Polar Radiant Energy in the Far-InfraRed Experiment (PREFIRE) will use two 6U CubeSats to continuously
10   measure spectral far-infrared (FIR) emissions for the first time in the modern satellite era. By strategically operating two
CubeSats in separate sun-synchronous orbits, PREFIRE will achieve frequent orbit resampling ("intersections") that afford
insights into the underlying polar processes that modulate FIR emissions. These orbit intersections are integral to PREFIRE
science and will likely feature prominently in future CubeSat missions, motivating methods to characterize resampling
distributions. In this study, we develop new methods to locate orbit intersections and extract co-located pixels within
15   crossovers. Such methods are applied to simulated PREFIRE orbits to characterize the spatial and temporal distribution of
hypothetical PREFIRE intersections and identify the subset with short revisit times that can be used to inter-calibrate the
PREFIRE sensors. The analysis confirms that hundreds of intersections are anticipated each day, with the majority (> 75%)
occurring poleward of 66.5°. Inter-calibration intersections are concentrated between 72° and 78° N/S and will be used to
monitor changes in spectral differences between PREFIRE sensors.

20   Generalizing the analysis to pairs of polar orbiting CubeSats with different equatorial crossing times, we conclude
that the second CubeSat nearly quadruples the number of total intersections available for polar process studies. Spatial and
temporal resampling coverage is clearly enhanced when more than one CubeSat is deployed, securing greater latitudinal
representation and more diverse time differences between crossovers. The spatio-temporal profile of intersections between
CubeSats varies with the relative offset in their equatorial crossing times. Further, when two CubeSats are placed at different
25   altitudes, we find that their intersections exhibit time-varying, cyclic coverage, significantly increasing latitudinal coverage
relative to two CubeSats placed at identical altitudes that resample each other in constant latitude bands. This study
ultimately illustrates some factors to consider when designing future CubeSat science missions and outlines methods for
conducting the associated trade studies.

30   **1. Introduction**

Thermal emissions at wavelengths between 15 and 100 μm (667 and 100 cm^{-1}), generally referred to as the far-
infrared (FIR), account for more than 40% of outgoing longwave radiation (OLR) at every point on Earth (L'Ecuyer et al.,
2021). Outgoing FIR is especially pronounced in cold or elevated regions like the poles and the Tibetan Plateau, peaking at

over 60% in Antarctica during austral winter (L'Ecuyer et al., 2021). Despite their large contribution to the global energy

35 budget, FIR emissions have not been systematically, globally constrained owing to a lack of direct FIR observations (e.g., Harries et al., 2008; Feldman et al., 2014; Palchetti et al., 2020; L'Ecuyer et al., 2021). In fact, almost no terrestrial FIR missions have been attempted since NASA's 1970–71 Nimbus-4, which achieved the first global narrow-band FIR measurements from space (Huang et al., 2014). It is worth noting that the InfraRed Interferometer Spectrometer (IRIS) aboard Nimbus-4 measured only up to 25 µm (Hanel et al., 1972). Subsequent Soviet missions Meteor-25 and Meteor-28

40 launched in 1976 and 1977, respectively, also measured wavelengths up to 25 µm (Kempe et al., 1980), but there have been no continuous observations of terrestrial FIR in the modern satellite era. Critically, emissions at longer FIR wavelengths (> 25 µm) are altogether uncharted.

This observational shortcoming can be attributed to several challenges unique to FIR spectra. Chiefly, the corresponding low photon energy traditionally mandated expensive supercooled detectors (L'Ecuyer et al., 2021) and long

45 integration times (Harries et al., 2008) to narrowly resolve outgoing FIR. Incomplete spectral measurements ultimately result in lingering uncertainties in Earth's thermal fluxes, and, by extension, the atmospheric greenhouse effect (AGHE). These uncertainties are compounded by persistent knowledge gaps concerning FIR emissivities, which have necessitated making assumptions based on observations in the mid-infrared windows (8–12 µm). These assumptions remain a source of error in radiative transfer models (Chen et al., 2014), resulting in non-negligible discrepancies in calculated top of atmosphere

50 (TOA) OLR, up to 10 Wm^{-2} in some regions (Huang et al., 2016). The extent to which such discrepancies impact energy budget reconstructions may be substantial, especially in sensitive areas such as the poles. For instance, comparing estimates of decadal mean annual surface flux from 2000–2009 reveals uncertainties ranging between 35–70 Wm^{-2} and 70–80 Wm^{-2} in the Arctic and Antarctic, respectively (L'Ecuyer et al., 2021). Reducing these uncertainties will require, among other things, systematic measurements in the FIR to a degree not yet seen in past Earth System observations.

55 The Polar Radiant Energy in the Far-InfraRed Experiment (PREFIRE) aims to address this observational gap by pioneering passive, moderate-resolution FIR measurements from space using nascent sensor technology deployed on two 6U CubeSats. PREFIRE will use these measurements to advance our understanding of AGHE in the poles and help constrain FIR emissivities for common polar surfaces. Together, the PREFIRE CubeSats, referred to as simply SAT1 and SAT2, will retrieve near-global TOA radiances from approximately 5 to 54 µm at a spectral resolution of about 0.86 µm. Launched in

60 May and June 2024, both satellites achieved altitudes of approximately 530 km in separate sun-synchronous orbits, with the mean local time of the ascending nodes (MLTAN) offset by approximately four hours. This configuration follows from the orbital trade study undertaken by Drouin et al. (2022), which found that equatorial separation between PREFIRE CubeSats would yield favorable high-latitude coverage.

Over the duration of the one-year baseline mission, PREFIRE measurements will be achieved via ambient-

65 temperature Thermal Infrared Spectrometers (TIRS), described in greater detail by Miller et al. (2023). The central wavelengths of the TIRS channels, listed in Appendix A for reference, are not identical across detectors but cover a similar spectral range. Either uncooled detector will continuously collect near-nadir observations, forming swaths composed of eight

disconnected scenes that extend roughly perpendicular to the motion of the subtrack. When projected onto Earth's surface, each scene will form footprints that are approximately 12 km wide and separated in the across-track direction by a gap

70 approximately double their width. Footprints overlap considerably in the along-track direction, such that nearly every six successive footprints will be partially co-located. Each TIRS will independently map Earth's complete emission spectrum and its seasonal variations.

Ultimately, a key strength of PREFIRE is the additional science afforded by two CubeSats. Although the mission's compact, fuel-free hardware naturally limit the mission duration overall, the ability to enlist multiple low-cost CubeSats

75 enables the strategic use of orbit resampling to investigate the processes that modulate Earth's emission, information critical for understanding climate forcings and feedbacks. Such resampling underpins the so-called "*PREFIRE intersections*" that occur when a CubeSat revisits a region previously sampled by either itself or the other satellite. Guided by the premise that the PREFIRE intersections will provide insights into the dynamic local conditions that influence polar energy budgets, this study seeks to develop methods for identifying orbit resampling and to employ them to investigate the plausible spatial and

80 temporal characteristics of the PREFIRE intersections. Methods to approximate orbit intersections and extract co-located pixels are detailed in Sect. 2. The character of PREFIRE intersections will be described numerically in Sect. 3.1, spatially in Sect. 3.2 and temporally in Sect. 3.3 and 3.4. An additional exercise is undertaken in Sect. 4 to demonstrate the utility of the intersections as a tool for inter-calibration. Finally, a brief comparison of resampling coverage for different equatorial crossing times is summarized in Sect. 5. Although satellite resampling is not unique to this mission, the spatial and temporal

85 pattern of the PREFIRE intersections is integral to achieving its process-related science goals. Further, as constellations of low-cost CubeSats are increasingly used to target specific science objectives (e.g., Stephens et al., 2020), we anticipate a greater need for similar strategic resampling considerations in the future.

2. Methodology

90 During the last two decades, the scientific value of intersections between satellites has been increasingly recognized, motivating techniques to predict and detect their occurrence. Considerable attention has been focused on simultaneous nadir overpasses (SNOs) in particular, which have been used for in-orbit calibration since 2001 (e.g. Cao et al. 2002; Heidinger et al., 2002; Cao et al., 2005; Wang et al., 2007; Chander et al. 2013). Early versions of these methods predicted coincident footprints by generating simulated orbits and selecting sequential pairs of pixels whose Great Circle

95 distance is less than a fixed threshold (Cao et al., 2004). Variations of the SNO method have followed, with different strategies for classifying co-located pixels. Iacovazzi, Jr. and Cao (2008) found that errors in SNO-based passive microwave calibration vary depending on whether co-located pixels are determined using simple proximity matchups or bilinear interpolation.

Nagle et al. (2009) show that two orbits must intersect if the scalar product of their end points (converted from

100 latitude/longitude coordinates to position vectors) are positive. In the same study, two approaches are defined for

determining whether a target field of view (FOV) is overlapped by pixels from an independent orbit. Their quasi-elliptical approach treats the target FOV as an ellipse and defines overlapping observations as co-located if their distance from the center of the target FOV is less than either the semi-minor axis or an intermediate threshold (Nagle et al., 2009). The quasi-conical approach treats the target FOV as a conical projection from the satellite and considers overlapping pixels co-located

105 if the angular difference between the slant ranges of both FOVs is less than the angular half-width of the target FOV (Nagle et al., 2009). Alternatively, recent adaptations of satellite data fusion studies have extracted co-located pixels using k-d trees (e.g., Weisz and Menzel, 2019; Anheuser et al., 2020), which are based on algorithms described in Bentley (1975) and Freidman and Bentley (1977).

Given the standardization afforded by emerging CubeSat platforms, this study introduces new methods that use

110 simple nearest-neighbor pixel matching to standardize orbit intersection analysis and the process of extracting co-located pixels. Although these methods are initially developed to support PREFIRE applications, they may broadly guide future CubeSat missions to promote consistent co-location strategies going forward.

2.1 Identifying intersections

2.1.1 Simulated PREFIRE orbits

115 Absent real orbit data during mission planning, simulated orbits can be generated to facilitate an analysis of plausible intersections. To emulate the PREFIRE mission configuration, two continuous months of orbits were simulated for both satellites using the Simplified General Perturbations No. 4 (SGP4), a duration taken to be sufficiently long to capture longer-term patterns, if any. Each orbit was assigned a hypothetical timestamp over the duration extending from June 28 to August 28, 2021. For every simulated orbit, hereafter referred to as a "granule," the date, UTC time, and latitude and

120 longitude for each scene was stored in a single NetCDF file (Rew and Davis, 1990). In keeping with the orbit parameters targeted in the mission, the granules used in this study were prescribed sun-synchronous orbits. Moreover, an equatorial separation of eight hours, a candidate orbit configuration during early mission planning, was chosen for this study. Two additional assumptions influenced the definition of the satellite altitudes. First, it was assumed that neither CubeSat will exactly achieve the targeted altitude, an assumption nurtured by the lack of fuel with which to raise or lower the spacecrafts

125 in orbit. Second, we assumed the satellites would not achieve identical altitudes. As such, we granted CubeSat 1 an altitude of 538 km and CubeSat 2 an altitude of 525 km. Table 1 summarizes the configurations of the simulated orbits. Constant drag was also applied to both CubeSats based on observed drag during the Time-Resolved Observations of Precipitation structure and storm Intensity with a Constellation of Smallsats (TROPICS; Blackwell et al., 2018). For simplicity, we used the *BSTAR* parameter for a TROPICS CubeSat at approximately 525 km.

Orbit type	Sun-synchronous
SAT1 altitude	538 km
SAT2 altitude	525 km

SAT1 MLTAN	0800 UTC
SAT2 MLTAN	1600 UTC

130 **Table 1 lists the orbit configuration prescribed in the simulations analyzed for this study.**

2.1.2 Fourth-scene method

In principle, identifying intersections requires comparing hundreds of thousands of pixels for every pair of orbits. To optimize the process, we consider only the fourth scene of each granule. This approximately locates the center of each intersection by determining where the interior scenes of two orbits are co-located.

135   It is sufficient to compile general sampling statistics by treating each scene as a point represented by its center, so, unless otherwise indicated, the coordinates of each scene correspond to the latitude and longitude of its center. Representing footprints as simplified objects enhances computational efficiency (e.g., Tobin et al., 2006). Additionally, owing to partial overlap in the along-track direction, computation time is reduced by a factor of six by skipping every six along-track segments for any pair of orbits. Further time savings are realized by dividing every granule into northwestern, northeastern,

140 southwestern, and southeastern segments and further binning pixels into 10° longitude bands for each regional segment. This allows regions for which intersections are not possible to be quickly discarded.

Since the TIRS swath extends some 200 km across, orbit intersections are properly detected when the fourth scenes of two granules are *sufficiently close*. There is some freedom in selecting a suitable separation for defining intersections. At the upper bound, one could adopt the dimension of the TIRS swath. In practice, however, a much smaller threshold is desired

145 to approximate the center of an intersection rather than simply any point contained therein. On the opposite end, the smaller the selected threshold, the greater the likelihood of failing to identify an intersection altogether. To navigate between these extremes, we discard every pair of fourth footprints greater than 25 km apart. All pixel pairs within 25 km are retained and the pair yielding the smallest distance is selected as the probable intersection center. To avoid duplicates, any newly flagged pixel pair found to occur within 500 km of a previously identified intersection is discarded as a duplicate intersection.

150   For every intersection, an "intersection ID" is generated that contains the CubeSat number, granule number and along-track position for the flagged scenes for both orbits. Additionally, the simulated timestamp for either granule is retrieved, and the time difference calculated and retained. Since PREFIRE intends to characterize the FIR spectral signatures of polar processes (e.g., ice sheet melt, cloud cover change, water vapor fluxes) that occur on a range of timescales, our method captures both the spatial and temporal coverage afforded by the mission's resampling. Figure 1 illustrates how our

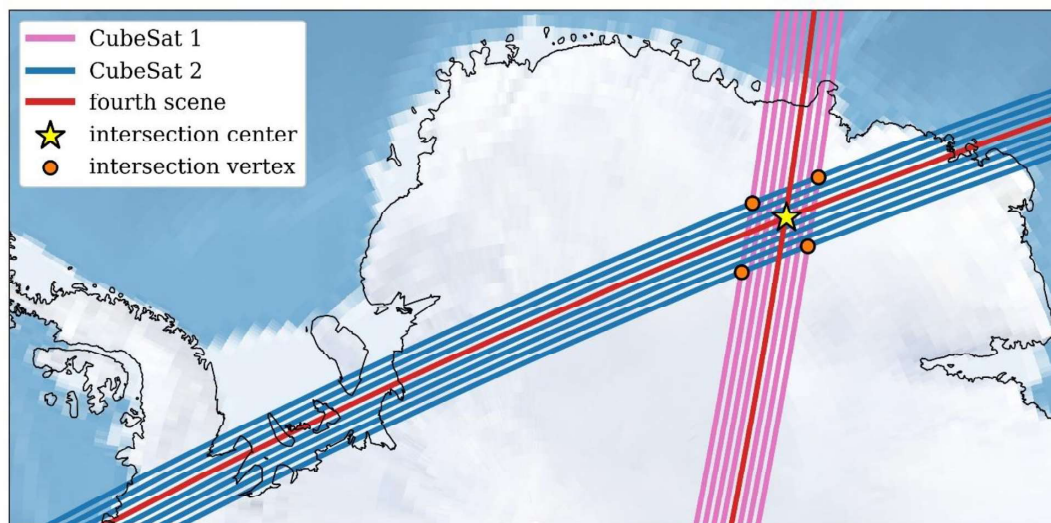155 simple method identifies the approximate center of an intersection over interior Antarctica.

Figure 1 illustrates the fourth-scene method for an arbitrary simulated Antarctic intersection.

160   Using the fourth-scene method, we identified all intersections within a rolling 48-hour window over the two-month period, starting with the granule timestamped at +48 hours of the first available granule and ending with the granule timestamped at −48 hours of the last available granule. Hereafter, the elapsed time between sampling, or *time difference,* is denoted Δt. Note that a time difference is relative to the granule being analyzed, so that a positive (negative) time difference implies that the granule being considered completed the earlier (later) crossover. This sign convention is arbitrary and may

165   change during the mission. This analysis separately investigates simulated intersections by a single PREFIRE CubeSat ("*self-intersections*") and intersections between PREFIRE CubeSats ("*SAT1–SAT2 intersections*").

2.1.3 Quality testing

           Systematic quality assurance was conducted to identify missed or duplicate intersections and relied largely on the observation that intersections come in pairs, such that every PREFIRE orbit has either two or four intersections. As such, the

170   number of intersections between every combination of two orbits was enumerated. If an odd number of intersections was identified for a particular orbit pair, then that pair of orbits was flagged for review.

           Missed intersections were rare and primarily occurred in the vicinity of the prime meridian. To account for intersections missed, an iterative process was undertaken to repeat the fourth-scene method with more lenient requirements. For the first iteration, the distance threshold was increased from 25 km to 40 km. Any remaining missed intersections were

175   then identified by repeating the process but testing every along-track segment rather than skipping every six as before.

Extending the distance threshold and considering every along-track segment, though computationally much slower, was sufficient to identify all remaining missed intersections.

Duplicate intersections were found in the vicinity of the equator. This follows from the fact that equatorial intersections occur near the terminus of granules, such that it is possible to identify a single equatorial intersection once near the end of one granule and then again near the beginning of the next successive granule. Duplicates were thus identified by retrieving the time difference and coordinates for all intersections. Intersections with common coordinates and timestamps < 90 minutes apart (the approximate duration of a single orbit) were flagged as duplicates and removed from the final analysis.

2.1.4 Intersections v. repeating ground tracks

There were numerous orbit combinations that yielded partially or fully repeating ground tracks. This phenomenon, described in previous literature (e.g., Rees, 1992), may yield valuable information content, but repeating ground tracks were excluded from this study. Instead, we required that resampling regions exhibit relatively compact diamond shapes to be classified as intersections. It can be shown that the equatorial proximity of two orbits and the spatial extent of their resulting intersections are positively correlated. All combinations of orbits were therefore tested for proximity by measuring the distance between the granules near the equator, using the tenth along-track segments of either granule to approximate their respective equatorial positions. If the fourth scene of the tenth along-track segment for two orbits was less than 700 km apart, a threshold chosen following qualitative testing, then their overlap was considered too elongated, and the granule pair was removed from this study.

2.2 Defining intersections

2.2.1 Diamond vertices

Having identified intersection centers, we define each intersection by extracting all remaining co-located pixels from a resampling region. Our method employs the same simple distance calculations underpinning the fourth-scene method, beginning with the four pixels that form the vertices of the diamond-shaped intersection (Fig. 1). Note that each vertex represents a pair of exterior pixels that are approximately co-located. The first vertex corresponds to the first scenes of the overlapping granules, another corresponds to the overlap between their eighth scenes, a third constitutes the overlap between the first scene of one granule and the eighth scene of the other, and vice versa for the remaining vertex. To identify vertices for any arbitrary intersection, we extract segments of the first and eighth scenes from each granule centered on the along-track index of the intersection center. Since intersections become more elongated as the equatorial proximity of their orbits increases, orbits that are close together (as given by testing the distance between the tenth along-track segments of an orbit pair) require longer segments. Depending on this proximity, segments of the first and eighth scenes range from ± 150 tracks to ± 600 tracks with respect to the intersection center. All pairs located within 15 km of each other were flagged as possible vertices and sorted in ascending order of distance. Indices are then identified as follows:

1. For each intersection, the pair of pixels with the absolute minimum separation is always taken to be one of the vertices.

2. The remaining three vertices are identified iteratively by further considering the distance between the remaining pixel pairs and the other vertices. Vertices are always located at separate regions of an intersection and should therefore never be near one another. The second vertex is found by identifying the closest remaining pixel pair that does not land within 25 km of the first vertex.

3. This process is repeated to find the third and fourth vertices, finding the closest remaining pixel pairs that are not within 25 km of any other vertex.

4. Once four pairs are identified, one vertex for each orbit, the process concludes, and each pair is taken to represent the four vertices of a particular intersection region.

2.2.2 Interior pixels

With the vertices identified, the next objective is to extract the remaining co-located pixels. In theory, we can employ existing geometry packages to achieve this, provided that any combination of vertices yields a "valid" polygon. In reality, however, available routines perform unreliably owing to the highly variable orientation of the intersections. It was shown that some intersections are not perceived as valid polygons and interior pixels were inaccurately extracted. Further, the across-track discontinuities imply that many footprints located between the vertices of one orbit are not strictly co-located with footprints from the other. As a result, a new method is required that takes this into account.

This method begins with the observation that the perimeter of an intersection comprises segments of the first and eighth scenes that connect two vertices, with each orbit contributing two bounding segments. It naturally follows that all interior pixels are contained within the sequence of tracks bounded by the lower and upper tracks of the perimeter. The previous method described in Sect. 2.2.1 yields the segments of the first and eighth scenes that form the intersection boundary. To identify all other pixels within the intersection, we need only consider scenes 2–7.

As before, we subselect each of the remaining six scenes, this time between the lower and upper track of the perimeter, and then use their distances with respect to the first and eighth scenes of the opposite granule to find where each interior scene intersects both exterior scenes. The full intersection region is then represented by the segments of each scene, starting from the nearest pixel corresponding to scene 1 of the other granule and extending to the nearest pixel corresponding to scene 8, including the segments between vertices that were found previously. This process yields an inclusive sample of "interior pixels."

Strictly co-located footprints (hereafter, "common pixels") of an intersection are important for numerous applications since they facilitate more direct comparisons between the two sensors. To identify common pixels, we compute the distances between every pair of scenes from both sensors within the intersection. The closest pixel pairs indicate where each of the eight scenes of the first granule approximately intersect the eight scenes of the other, resulting in 64 pixels per

orbit that share approximately the same coordinates. Figure 2 summarizes the methods outlined in this section and specifies

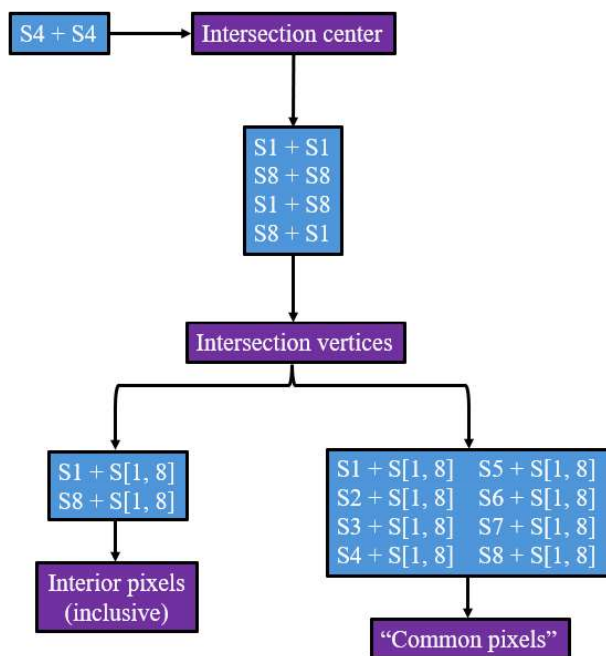240   the scene-wise overlaps that define each intersection feature.

Figure 2 illustrates our sequential method to extract intersection pixels. Purple boxes list intersection features, whereas blue boxes specify the corresponding scene combination(s) used to derive them. In the context of scene

245   **combinations, it is implied that we are referring to their point of convergence. The format SX + SY is used to denote overlaps between scene X of one granule and scene Y of the other. Alternatively, SX + S[Y, Z] designates overlaps between scene X of one granule and all scenes ranging from Y to Z of the other. For either the interior or common pixels, some combinations are accounted for in preceding steps.**

2.3 Conceptual example

250   When processes like sea ice melt, cloud cover change or moisture flux are captured by a PREFIRE intersection, comparing the spectral radiances (I_λ) measured during each crossover will help us constrain how such processes modulate outgoing FIR. Relative spectral differences are therefore central to the mission's resampling strategy, and it will remain a top priority to continually inter-calibrate TIRS1 and TIRS2 to ensure their spectral differences represent changes in observed scenes. To illustrate inter-calibration using the methods defined previously, we consider the special case of an intersection

255   with a marginal time difference. In the event of on-orbit instrument calibration drift, we require an approach to identify impacted measurements quickly. Short Δt intersections present an opportunity to develop a broad, open-ended approach to PREFIRE inter-calibration. The technique should reliably flag spectral differences between CubeSats that result from drift rather than changes in underlying conditions. Two complicating factors must guide our approach: First, recall that the channels for TIRS1 are centered on different wavelengths than TIRS2. Additionally, the spectral response functions
260   (SRFs) are both instrument- and scene-dependent. It follows that, provided identical conditions, each CubeSat will register somewhat different spectra even in the absence of instrument drift. As such, our technique must anticipate a baseline offset between CubeSats and monitor changes in time relative to this baseline from regular, short intersections while controlling for scene conditions. Varying differences between specific scene pairs imply drift and can be flagged accordingly.

It follows that the collection of shortest intersections between the PREFIRE CubeSats are ideal candidates for inter-
265   calibration. The conceptual case presented here corresponds to a SAT1–SAT2 intersection with a rapid time difference of less than three minutes. Although the true lower bound on resampling time may be greater operationally, this case demonstrates a general procedure that will guide calibration, and it can be adopted regardless of the degree of fidelity between the simulated and actual PREFIRE orbits.

As shown in Fig. 3 (left), this intersection is centered near 74.88° S, 107.35° E in East Antarctica. Figure 3 also
270   shows hourly skin temperature and TCWV from the Goddard Earth Observing Systems (GEOS) for Instrument Teams (GEOS-IT), courtesy of the Global Modeling and Assimilation Office at the NASA Goddard Space Flight Center. Both variables have been interpolated to each of the common footprints derived for this intersection and interpolated in time to represent conditions between hourly timesteps.
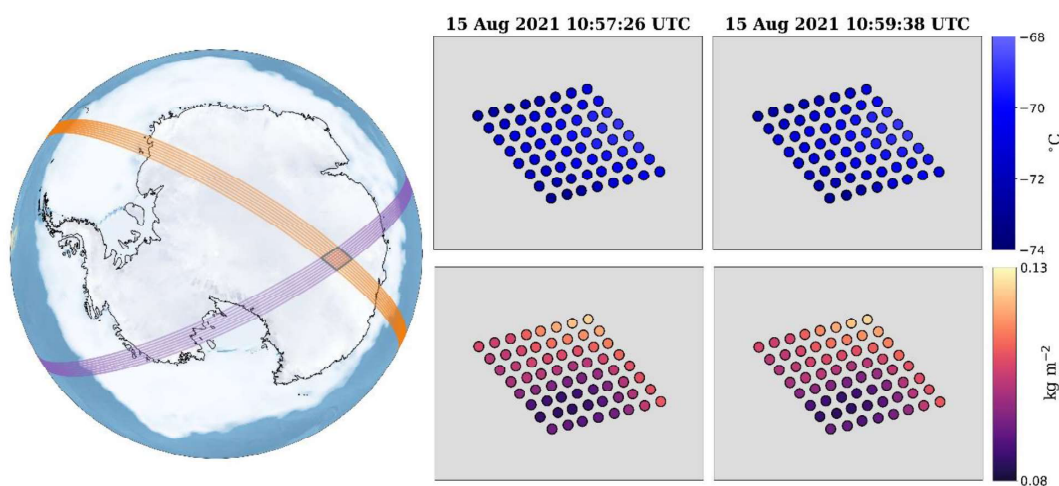

275

Figure 3 shows the constituent granules forming the intersection featured in our conceptual case (left) as well as GEOS-IT skin temperatures (top right) and TCWV (bottom right) interpolated to common pixels of either granule during the first and second crossover. The first and second crossover are shown on the left and right, respectively.

280   By design, the selected intersection should exhibit negligible scene differences between the first and second crossover just three minutes later. We confirm this by plotting GEOS-IT skin temperature and TCWV for every common pixel per granule. This is respectively shown in the top and bottom of Fig. 4. Strong overlap between the pixels of the first and second crossover for either variable confirms conditions are approximately static between observations.
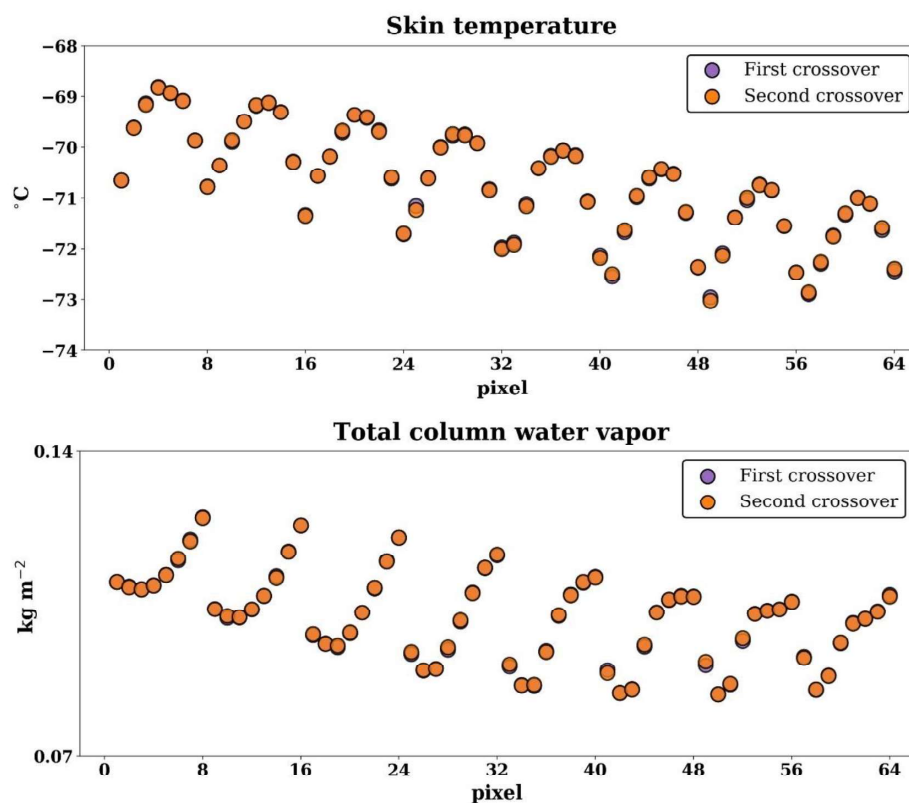
285

Figure 4 compares GEOS-IT skin temperature (top) and TCWV (bottom) for the common pixels during the first and second crossover. We note that values for the first crossover are hardly visible owing to the strong agreement between sampling.

290   An approach for using such intersections to monitor the inter-calibration of the PREFIRE CubeSats will be further articulated in Section 4. Given that each scene has a unique SRF, the technique considers all pairs of scenes between the CubeSats individually. This method, which is demonstrated using simulated clear-sky radiances, I_λ, for both granules below, is as follows: For each scene of TIRS1, calculate ΔI_λ with respect to each of the eight scenes of TIRS2 for a representative sample of channels. Due to the channel offsets on each TIRS, we match the channels with the closest central wavelength for

295   each sensor. Close intersections in the first month of the mission will be used to generate baseline spectral differences for all scene pairs against which statistics from subsequent months can be compared throughout the duration of the mission. We provide a simple conceptual example of drift below by arbitrarily increasing I_λ by 10% for a single TIRS2 scene.

2.4 Methods for optimizing equatorial crossing times

With an eye toward informing future CubeSat missions, we also generalize the results to assess the relationship

300   between equatorial crossing times and resampling coverage. To do so, our analysis identifies simulated SAT1–SAT2 intersections for four pairs of hypothetical CubeSats at equal altitude (525 km), with each pair representing a 2-hour, 4-hour, 6-hour or 8-hour MLTAN offset scenario. Each scenario is achieved by retaining the simulated orbits of one PREFIRE CubeSat and then adjusting the longitude coordinates 30°, 60°, 90° or 120° to represent orbits for a hypothetical second CubeSat. We then identify all SAT1–SAT2 intersections ±12 hours for approximately one week of orbits. As before, we

305   restrict our analysis to relatively compact resampling regions by discarding orbit pairs located within 700 km of each other at the equator, again calculating this distance using the fourth scene of the tenth along-track segment. Quality testing was undertaken in the same manner as described in Sect. 2.1.3.

3. Spatial and temporal analysis of PREFIRE intersections

310   The method described in Sect. 2.1.2 was applied to the two-month sample of simulated orbits, and all intersections within a rolling 48-hour window were identified and categorized by latitude and Δt. Since the spatial and temporal patterns of SAT1 and SAT2 self-intersections are roughly identical, we only show results from SAT2 self-intersections and SAT1–SAT2 intersections in the spatial (Sect. 3.2) and temporal (Sect. 3.3) analyses. Additionally, given the importance of shorter-term resampling for PREFIRE's science objectives, we prioritize intersections with $|\Delta t| < 12$ hours for much of this paper.

315   **3.1 Numerical distribution of simulated intersections**

The number of intersections identified in three different sampling windows are presented in Fig. 5. For intersections ±48 hours, our analysis identified more than 200,000 combined intersections over the two-month period, with SAT1 self-intersections, SAT2 self-intersections and SAT1–SAT2 intersections contributing 53,402, 55,398 and 109,790, respectively. Not surprisingly, the number of intersections is roughly halved when only those within ±24 hours are considered and halved

320 again when intersections within ±12 hours are considered. Self-resampling for either CubeSat accounts for approximately one-quarter of the total, and there are twice as many SAT1–SAT2 intersections as self-intersections for a single CubeSat. Taken together, the value of having two CubeSats is clear: A second CubeSat results in about four times as many intersections as one CubeSat alone.
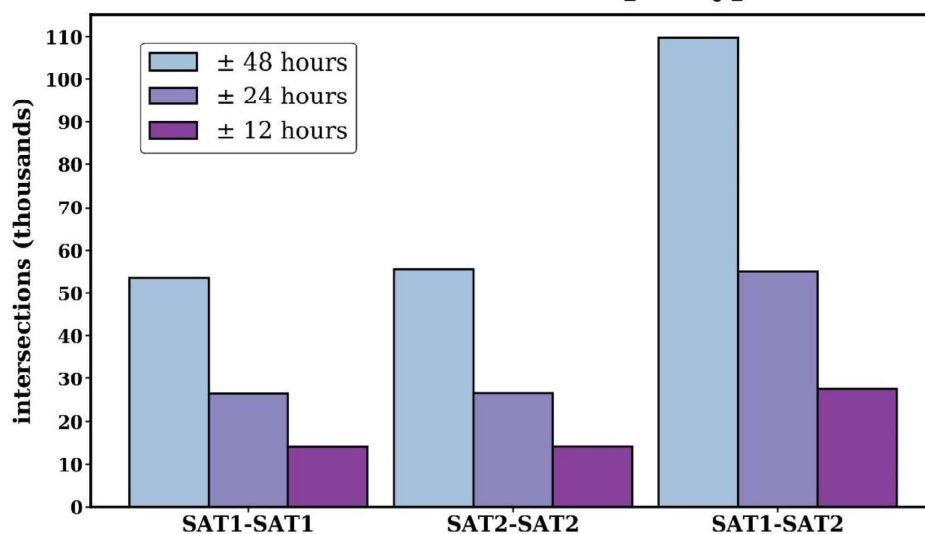
Figure 5 lists the number of intersections over the simulated two-month period for each intersection type and for
325 **three temporal categories. Counts may differ during the mission.**

The mean, minimum and maximum number of daily intersections and their standard deviation is summarized in Table 2. There are about 240 daily self-intersections for a single CubeSat with a daily minimum and maximum of 240 and
330 247, respectively. Interestingly, about 180 or ¾ of those will be polar intersections (poleward of ±66.5°). For the orbits simulated, we expect an average of over 470 global SAT1–SAT2 intersections per day, nearly double the number of global self-intersections for a single CubeSat. Note, however, that day-to-day variations are larger for SAT1–SAT2 intersections than for self-intersections, varying from 451 to 523. Of these, roughly 360 will occur in polar regions.

	Mean daily	Min daily	Max daily	Std. dev.
SAT1–SAT1	242 (181)	240 (180)	247 (186)	2.1 (2.1)
SAT2–SAT2	243 (182)	240 (180)	247 (186)	2.5 (2.6)
SAT1–SAT2	474 (362)	451 (330)	525 (403)	21.4 (15.9)

335   **Table 2 shows mean, minimum and maximum daily intersections as well as the standard deviation for each intersection type. Values indicate global (polar) intersections, where 66.5° is used as the polar cutoff for either hemisphere. The number of daily intersections may differ during the mission.**

3.2 Spatial distribution of simulated intersections

Intersection coverage varies sharply depending on whether we consider self-intersections or intersections between CubeSats. Figure 6 shows the spatial distribution for SAT2 self-intersections in three broad sectors: low latitudes (0° N/S to

340   30° N/S); mid latitudes (30° N/S to 60° N/S); and high latitudes (60° N/S to 82° N/S). The distributions are symmetric between hemispheres with about one-eighth (12.5%) of intersections occurring in low latitudes and another one-eighth (12.5%) centered in mid latitudes. The majority of intersections occur in the high-latitude sector central to PREFIRE's polar science objectives, totaling approximately three-quarters (roughly 75%) overall. Figure 6 also confirms what the previous observations tacitly reveal: Self-intersections are anticipated within discrete latitude bands leading to latitudinal gaps in

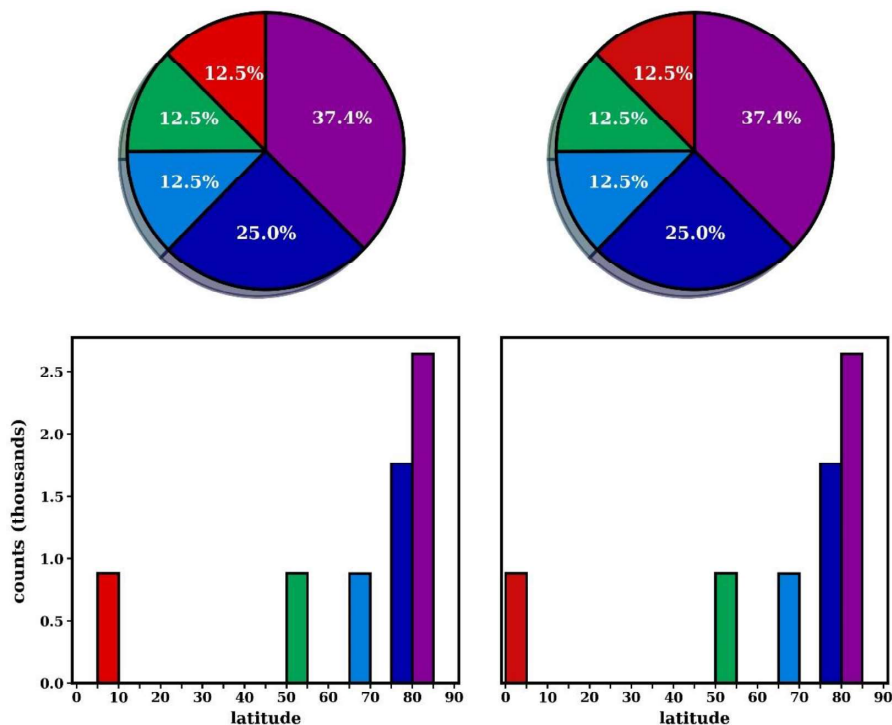345   coverage, particularly in low- and mid-latitude sectors.

Figure 6 shows the latitudinal distribution of SAT2 self-intersections based on the simulated orbits analyzed in this study. For completeness, the Northern and Southern Hemisphere are considered separately. Colors signify regional sectors, where warm colors denote low-latitude bins; greens denote mid-latitude bins; blues denote high-latitude bins, excluding the bin containing the maximum sampling latitude; and purple denotes the polar-most bin containing the maximum sampling latitude for either hemisphere.

This shortcoming is remedied when considering intersections *between* CubeSats. Figure 7 illustrates the hypothetical spatial distribution of SAT1–SAT2 intersections in each hemisphere, immediately underscoring the unique nature of this type of resampling. Whereas self-intersections occupy discrete latitude bands, SAT1–SAT2 intersections exhibit continuous coverage from the equator to our maximum sampling latitude. Despite this continuity, the nature of the polar orbit results in a majority of SAT1–SAT2 intersections being centered in high latitudes, just as we found earlier for self-intersections. In fact, over 75% of SAT1–SAT2 intersections are found at or poleward of $\pm 60°$, with the number of intersections increasing monotonically in the direction of either pole. Intersections are particularly dense near the maximum

360   sampling latitude, where we encounter roughly twice as many SAT1–SAT2 intersections compared to self-intersections for a single CubeSat.
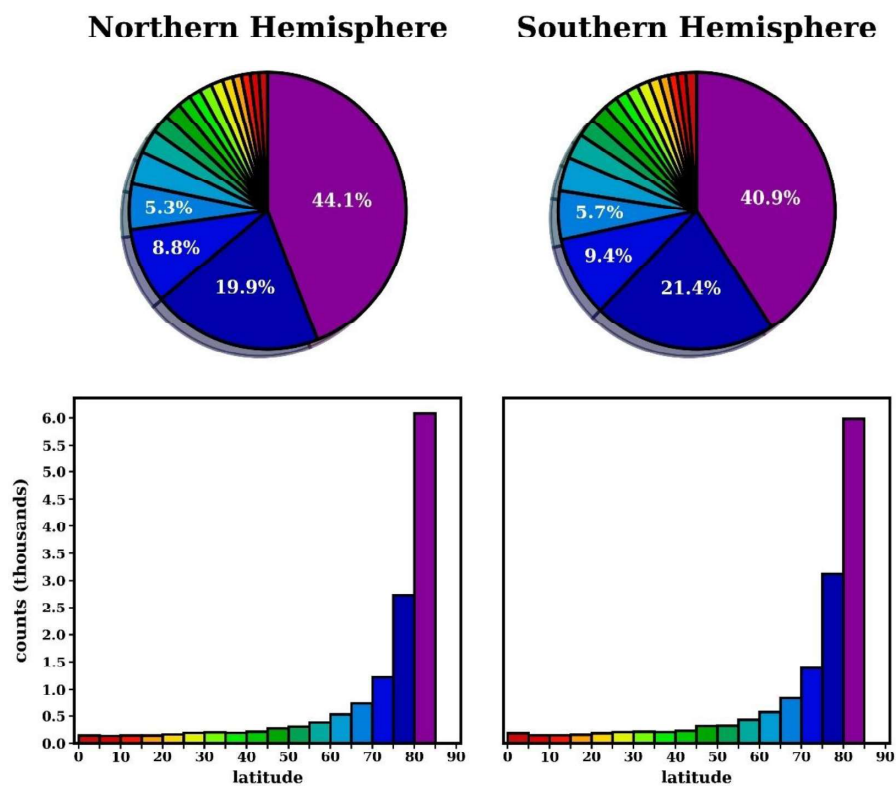

Figure 7 is the same Fig. 6 but for SAT1–SAT2 intersections. Note the y-axis is nearly double compared to Fig. 6.

365   **3.3 Temporal distribution of simulated intersections**

Integral to PREFIRE's investigation of the processes that modulate polar energy balance is the ability to sample a wide range of time scales. Figure 8 shows SAT2 self-intersections for a randomly selected CubeSat 2 granule. The centers of every self-intersection for the selected granule have been plotted, up to ± 12 hours. The number of self-intersections consistently total 32 per granule and exhibit patterns of decreasing Δt as we move toward either pole. Near the equator, Δt

370   hovers near our imposed upper limit of ± 12 hours. If we move poleward, we see a gradual fdecrease in Δt, reaching the theoretical minimum of about 1.5 hours (the orbital period) near the maximum sampling latitude. Additionally, self-

16

intersections are found in ascending-descending pairs. This implies that when we identify a discrete Δt on an ascending segment of an orbit, we can find a matching Δt on the descending segment of the same orbit, located in roughly the equal latitude in the opposite hemisphere. To avoid redundancy, we note that this ascending-descending pairing is observed for all
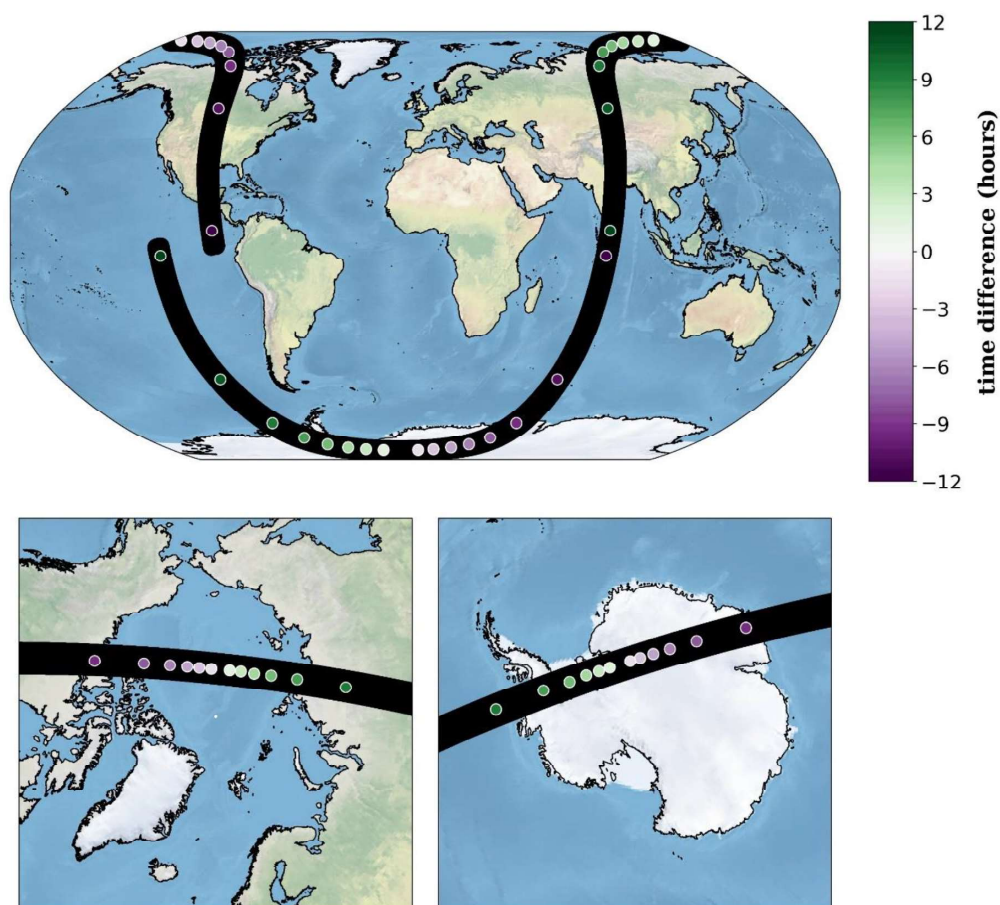375   intersection types. Moreover, a nearly identical temporal pattern was found for SAT1 self-intersections (not shown).


Figure 8 shows an arbitrary CubeSat 2 granule and the centers of all $\pm$12-hour self-intersections specific to that orbit. Each CubeSat 2 orbit yielded a constant number of self-intersections over the study period, totaling 32, as shown. Colors represent the elapsed time between crossovers.

380

These insights are key to interpreting statistics from all SAT2 self-intersections within ±12 hours over the two-month period, shown in Fig. 9. The pattern that emerges is one of time-invariant spatial coverage. In either hemisphere, we encounter eight distinct latitude bands containing intersections, with each band differentiated by a unique Δt. Our impression that intersections get shorter temporally as we climb to the highest latitudes is confirmed, with the longest and shortest intersections wrapped tightly in latitude bands near the equator and maximum sampling latitude, respectively. Although atmospheric drag on the satellite will eventually decrease its altitude and shift the latitude bands and time differences from the results shown here, these results highlight a significant limitation of self-intersections: In addition to gaps in coverage, specific timescales will only be observable at specific latitudes.
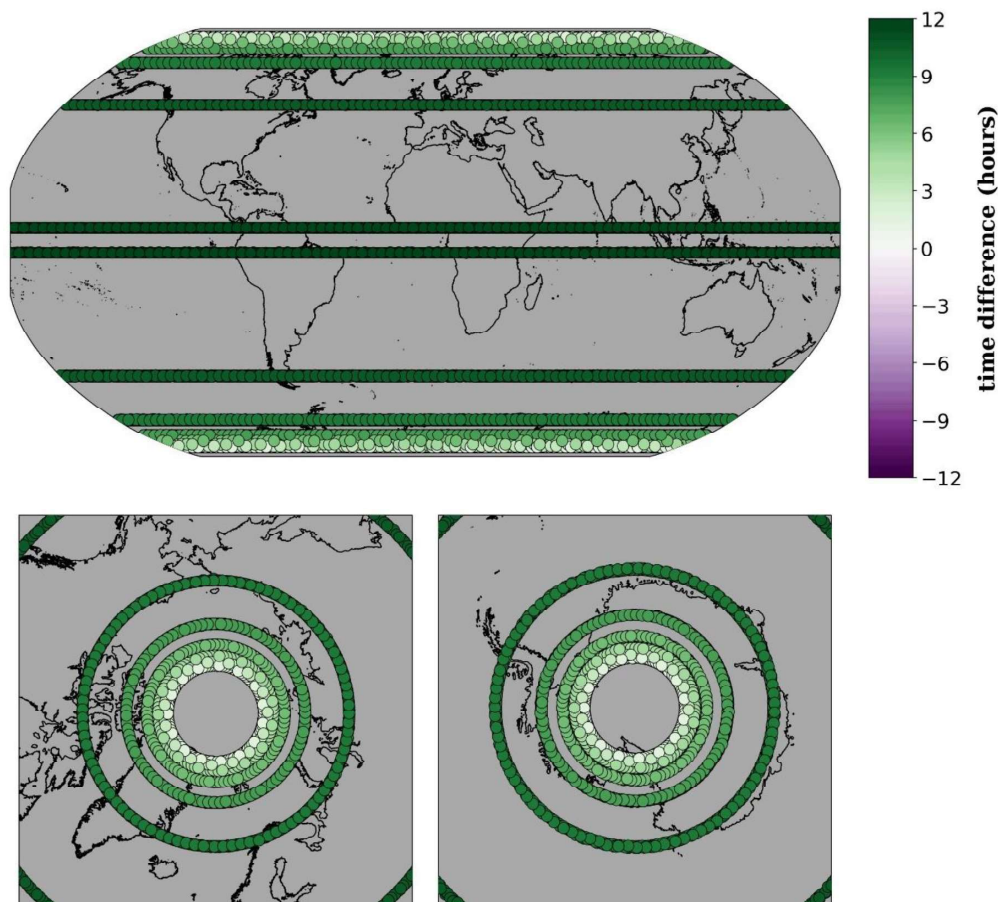
Figure 9 shows the centers of all SAT2 self-intersections observed over the simulated two-month period. Colors represent the elapsed time between crossovers.

Previously, we determined that SAT1–SAT2 intersections have relatively high variability on daily timescales, ranging by as many as 72 intersections per day globally. To understand this large spread, we narrow our scope and consider

395 the number of SAT1–SAT2 intersections per granule. Unlike self-intersections, the number of SAT1–SAT2 intersections per orbit is not fixed and varies from 30 to 34 intersections per granule. Figure 10 shows a CubeSat 1 granule that has 34 intersections with CubeSat 2 within ± 12 hours, thereby illustrating the upper bound per orbit. A cursory glance reveals notable temporal differences compared to self-intersections. Perhaps most obvious, Δt no longer decreases monotonically as we traverse from low to high latitudes. Instead, we find a staggering of time differences as we move poleward from the

400 equator. Starting with intersections at lower latitudes, Δt is near the median of our imposed 12-hour range. In the highest sampling latitudes, our attention is drawn to manifold Δt values, which signify fairly diverse temporal coverage in this vicinity. Notably, it is within these polar regions that we encounter Δt ranging from rapid (sub-orbit period) timescales up to our maximum of ± 12 hours.
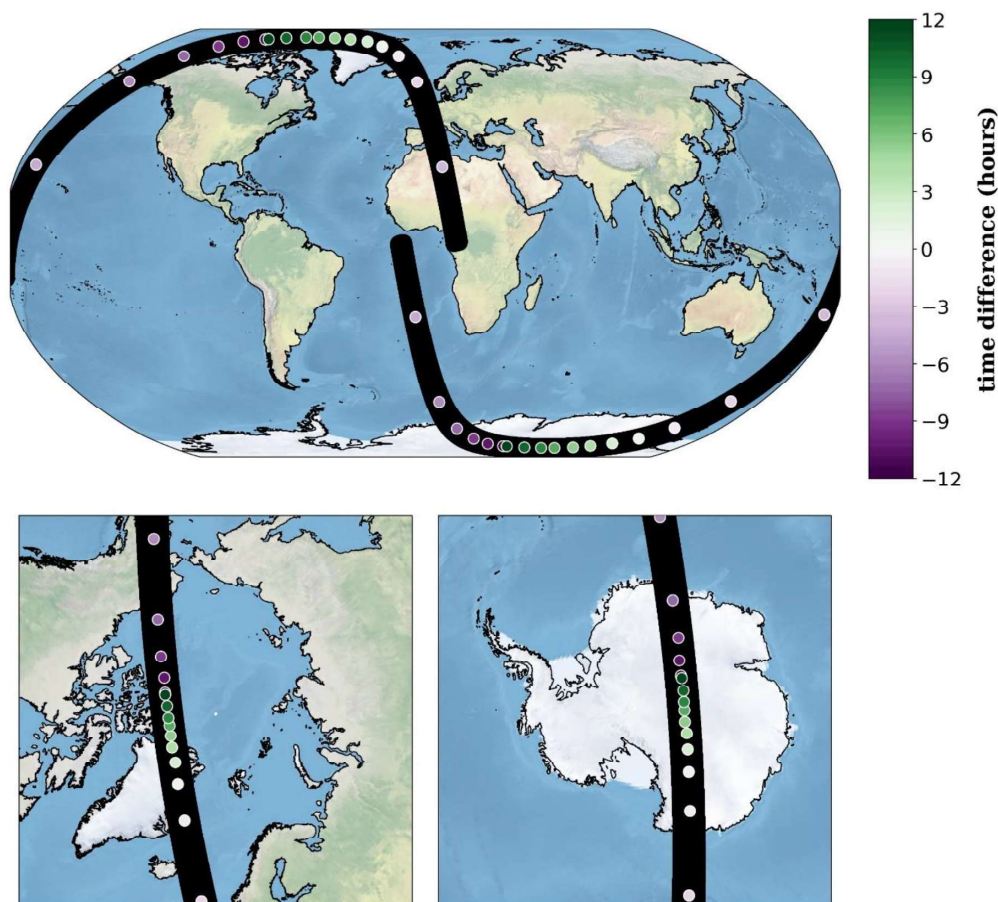
Figure 10 shows an arbitrary CubeSat 1 granule and the centers of all $\pm$12-hour intersections it encountered with CubeSat 2. The number of SAT1–SAT2 intersections per granule varied between 30 and 34 over the study period. This example illustrates the upper bound of SAT1–SAT2 intersections, totaling 34. Center colors represent the elapsed time between crossovers.

We can better qualify the differences in coverage relative to self-intersections by reviewing all SAT1–SAT2 intersections over the two-month period. The resulting mosaic of intersection centers, captured in Fig. 11, reveals a far more diverse temporal and spatial pattern to that encountered previously. In place of the discrete latitude bands we witnessed for self-intersections, we now find a cyclic patchwork of resampling. Coverage is no longer time-invariant, evident from the resonating network of Δt. Critically, dense and varied intersections in high latitudes imply that polar regions will be generously resampled between CubeSats, such that the impacts of polar processes on emission spectra can be studied.
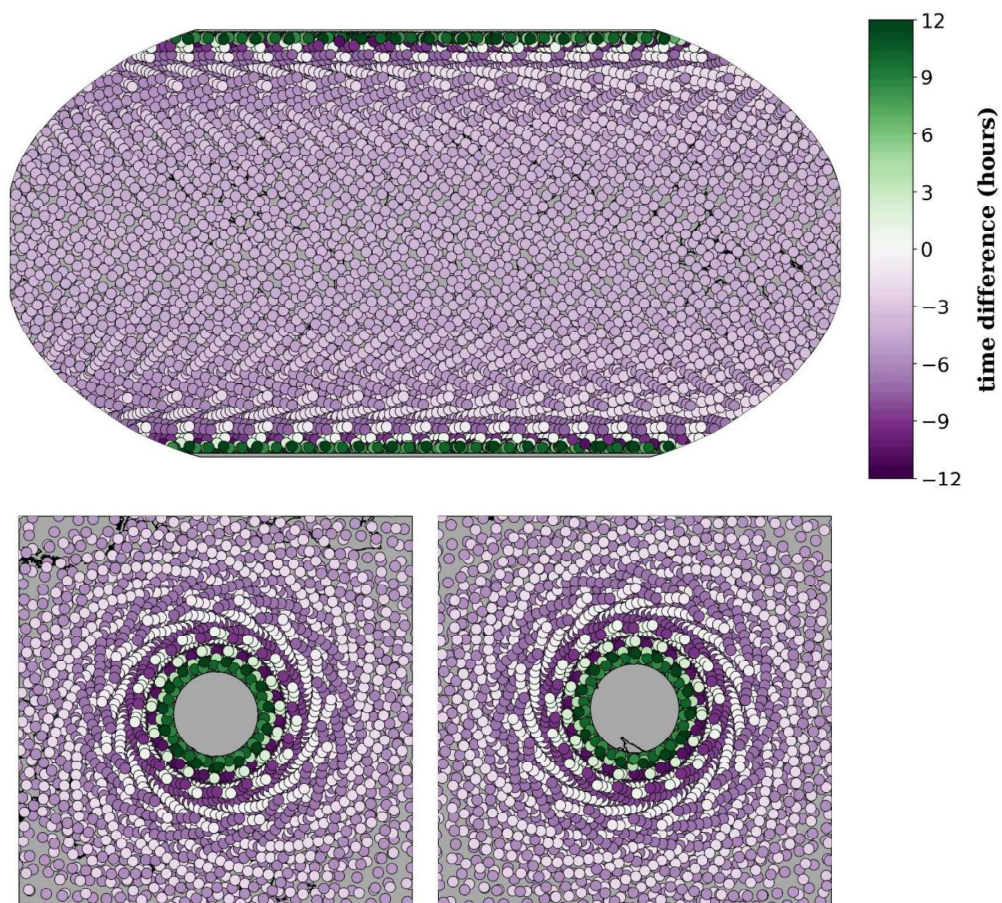
415

Figure 11 shows the centers of all SAT1–SAT2 intersections observed over the simulated two-month period. Colors represent the elapsed time between crossovers.

3.4 Simulated short-term revisits

420   Suppose the PREFIRE CubeSats register different I_λ when they intersect over a mutual region. To ensure we can interpret their spectral differences as true indicators of the impact of variable conditions on thermal emissions, we must account for any calibration differences between the instruments. Intersections over relatively homogeneous scenes with very short Δt will be integral to inter-calibrating TIRS1 and TIRS2 and are therefore characterized separately in this section.

Although such intersections are sometimes referred to as near-simultaneous nadir overpasses, this study hereafter refers to

425   them more generally as "short-term revisits" since they are never truly "simultaneous."

For an intersection to qualify as a short-term revisit useful for calibration, conditions should remain practically static from the first crossover to the second. In reality, therefore, the upper bound on Δt is not fixed and will vary depending on local conditions; however, we demonstrate this concept by examining all intersections within a threshold Δt of ± 30 minutes. The centers of intersections that satisfy this threshold are emphasized in red in Fig. 12. In the resulting mosaic, we

430   note meandering bands of short-term revisits that encircle the highest latitudes, extending from approximately 72° to 78° in either hemisphere. It follows that this latitude range would be appropriate to target for inter-calibration, with the important caveat that the precise location will need to be reassessed using true orbit altitudes after launch. The temporal pattern moreover implies that we achieve progressively shorter revisits as we move radially inward from the outermost latitudes of the range specified. The shortest revisits (darkest red) exhibit a minimum Δt near the center of the corresponding latitude

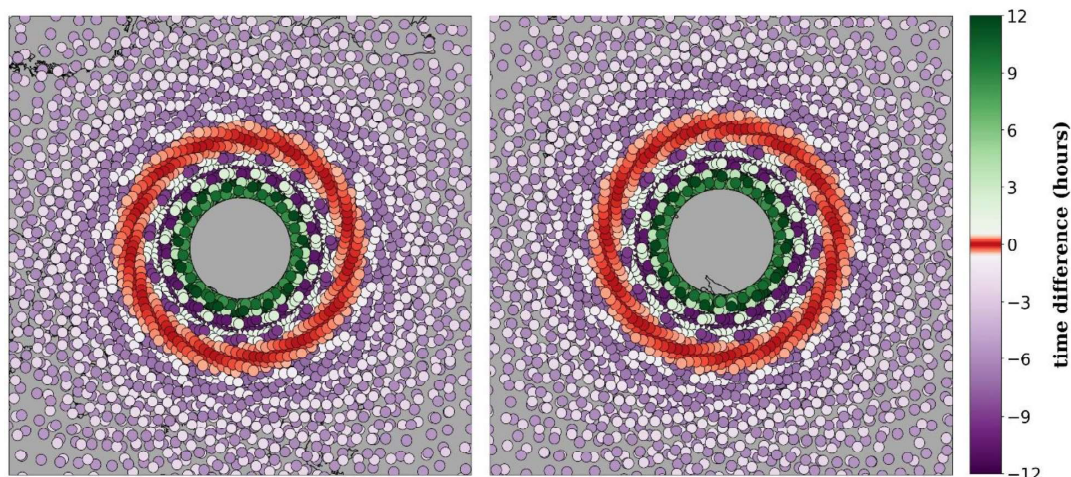435   range, approaching near-instantaneous timescales near $\pm 75°$.

Figure 12 is the same as Fig. 11 (bottom) but emphasizes intersections with Δt less than 30 minutes, shown in red. These intersections will be ideal candidates for inter-calibration.

440

4. Conceptual Calibration Approach

We now return to the conceptual example provided in Section 2.3 to illustrate a potential approach for inter-calibrating the PREFIRE CubeSats. Based on the preceding analysis, we anticipate that the PREFIRE CubeSats will achieve several intersections on rapid timescales, forming a set of short-term revisits like those characterized in Sect. 3.4. By virtue

445 of their tendency to sample static conditions, these short-term revisits lend themselves to developing a general strategy to identify instrument drift.

Figure 13 shows the mean I_λ for either crossover for the hypothetical intersection described in Sect. 2.3. Missing sensors channels are excluded. The shaded regions denote the maximum and minimum I_λ observed for either sensor in the intersection domain, confirming the homogeneity and static conditions in this intersection. More importantly, we observe

450 that the spectra for each instrument converge to lie on roughly the same (incomplete) Planck function despite the channel offsets between them. Although we do not interpolate between spectral gaps in this study, doing so would yield a full Planck function peaking near 15 µm. Thus, the mission's inter-calibration strategy may include generating mean I_λ for select short-term revisits and confirming whether their implicit Planck functions remain reasonably congruent.
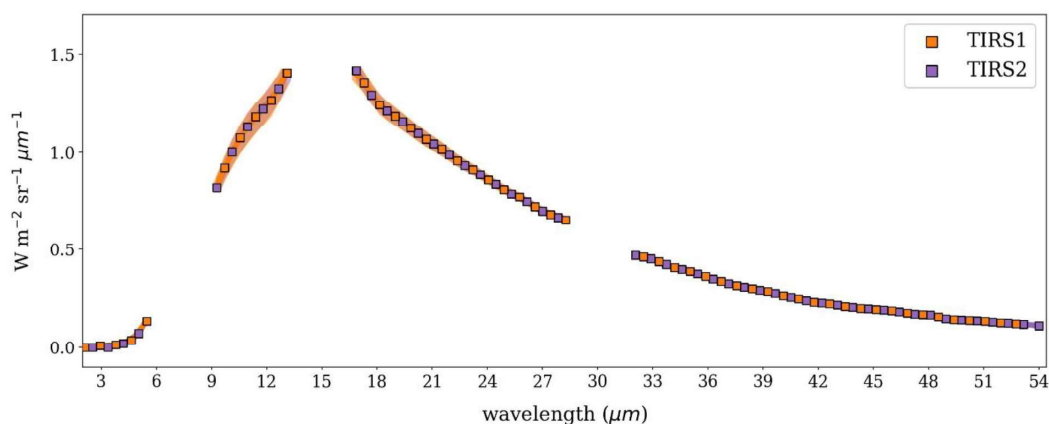

455

Figure 13 shows mean spectral radiances for all common pixels from either crossover. From Section 2.3, the sampled region has a mean skin temperature of -71°C and mean TCWV of 0.1 kg m^{-2}. As before, squares denote the central wavelengths for TIRS1 (orange) and TIRS2 (purple). Minimum and maximum spectral radiances are indicated for TIRS1 and TIRS2 pixels by the shaded orange and purple regions, respectively. Missing channels correspond to

460 **spectral gaps in either sensor. We note that the resulting spectra form (incomplete)Planck functions, as noted.**

Figure 14 shows ΔI_λ for each scene of TIRS1 compared to the eight scenes of TIRS2 for the hypothetical intersection described in Sect. 2.3. Select wavelengths between 6 and 40 µm are highlighted, but the approach could be applied to all TIRS channels. Recall that underlying conditions are effectively identical for either crossover, such that ΔI_λ results solely from the combined differences in channel centers and spectral response functions. What emerges from such a

465 comparison early in the mission is, therefore, the baseline spectral offset across instruments per scene, referenced to select wavelengths. For this exercise, we neglect specific values of ΔI_λ and instead focus more broadly on the degree of consistency

across scenes. Repeating this exercise for several intersections provides confidence in the reproducibility of the baseline offset between scenes on both sensors and provides an estimate of its variability.
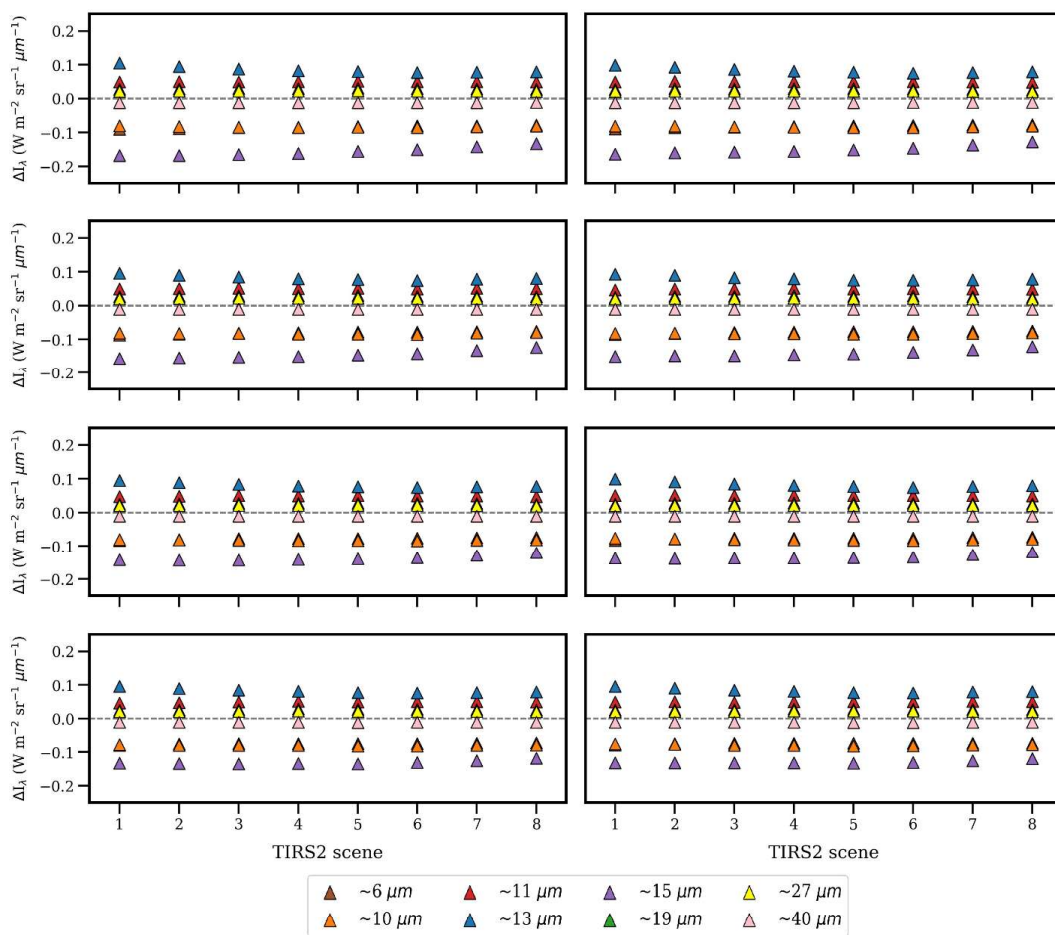
Figure 14 shows the nominal differences in spectral radiances between TIRS1 and TIRS2, where differences in each panel are taken with respect to a single TIRS1 scene and each TIRS2 scene. Triangles indicate the target wavelengths for which differences are computed. Note that the actual wavelengths for either sensor are not strictly identical to those targeted, such that the differences are calculated between the TIRS1 channels and the TIRS2 channels nearest the target wavelengths, which are not equal across sensors (hence the nonzero differences shown).

475   After establishing baseline conditions early in the mission, continuous monitoring of subsequent intersections should provide an early indication of instrument drift. As an idealized demonstration of sudden drift, we apply a 10% increase in I_λ to the eighth scene of TIRS2 and then recalculate ΔI_λ for the same scene. Figure 15 is the same as Fig. 14 but with our applied enhancement. Note that the affected scene is clearly distinguished by its unique ΔI_λ sequence. In this case, ΔI_λ is negative for every wavelength, a distinct feature of the impacted scene vis-à-vis the remaining seven. This "drift

480   signature" holds for all TIRS1 scenes. Although we do not quantify $\Delta(\Delta I_\lambda)$ in this study, we arrive at the premise that $\Delta(\Delta I_\lambda)$ is nonzero in the event of instrument drift and can therefore guide inter-calibration adjustments between PREFIRE CubeSats.
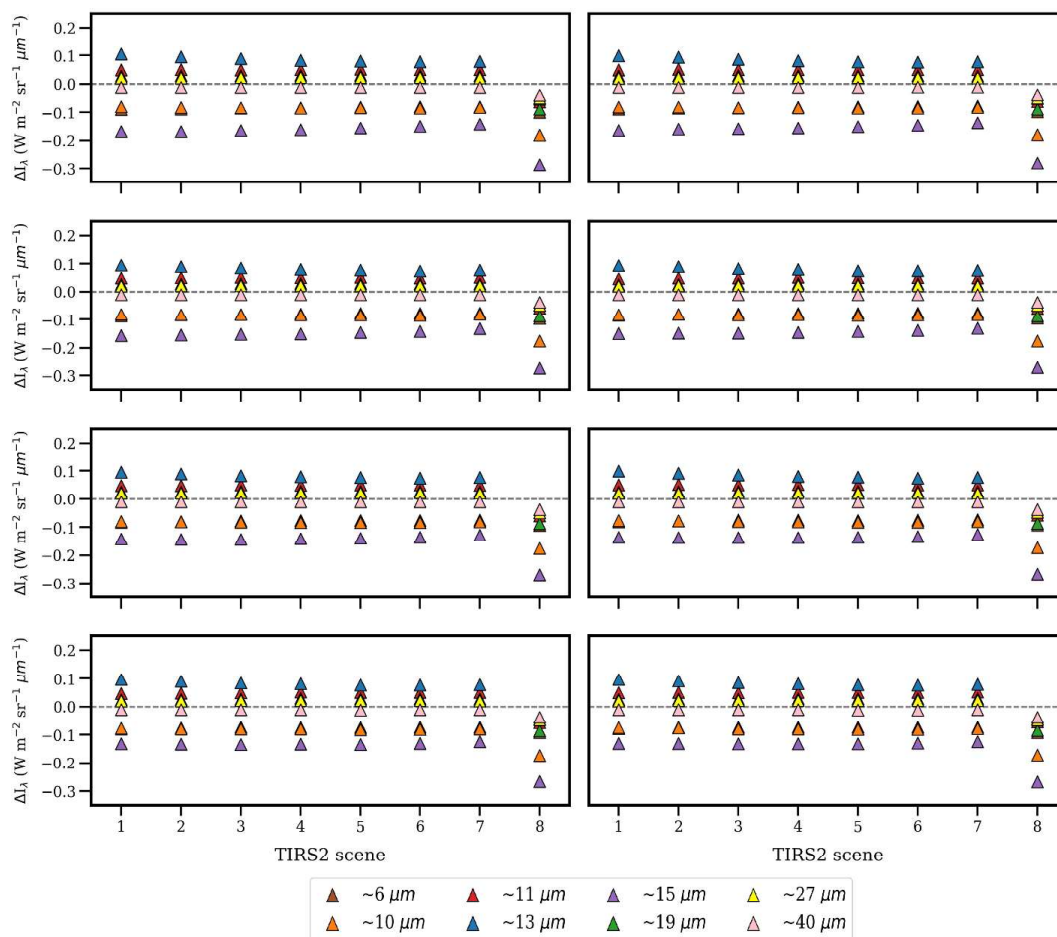

Figure 15 shows the differences in spectral radiances between TIRS1 and TIRS2 when idealized constant drift (10%) is applied to all channels of the eighth scene of TIRS2. As before, each panel represents differences between a single

25

TIRS1 scene and every scene of TIRS2. Note that the y-axis has been modified compared to Figure 14 to adequately show the spectral differences in the drift-affected scene.

5. Optimizing equatorial crossover times

Figure 16 illustrates the results for each MLTAN offset scenario described in Sect. 2.4. SAT1–SAT2 intersections exhibit discrete latitudinal coverage when both CubeSats share a common orbital altitude. This is an obvious departure from the coverage observed in the analysis in Sect. 3, for which different altitudes were prescribed to each satellite. This implies a critical finding: Time-varying resampling between two or more CubeSats requires placing the satellites at different altitudes.
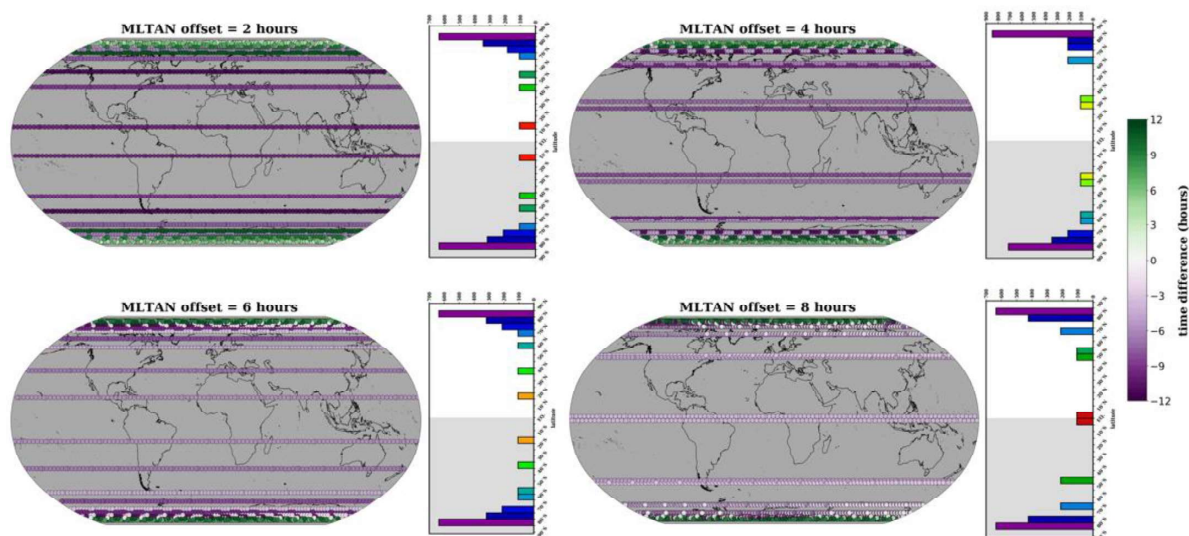

Figure 16 represents the global distribution of simulated SAT1–SAT2 intersections for each of the four MLTAN offset scenarios. Colors again represent the elapsed time between crossovers. Histograms are shown next to each global projection, with Southern Hemisphere latitudes shaded.

To summarize the spatial and temporal sampling across scenarios, we plot time versus latitude for the simulated SAT1–SAT2 intersections from each configuration in Fig. 17. For reference, Fig. 17 also shows simulated self-intersections. Our results confirm that unique SAT1–SAT2 resampling coverage can be achieved by adjusting the equatorial crossing time of one satellite relative to the other. Comparing the four scenarios, we find that low- and mid-latitude intersections tend to be

26

shorter for the scenarios with greater equatorial separation between CubeSats. There are also subtle spatial shifts across scenarios, with Δt near our upper and lower bound shifting poleward and equatorward, respectively, with greater MLTAN offset. Although SAT1–SAT2 resampling enhances intersection coverage in each scenario, observers will note strong spatial

505 and temporal agreement between self-intersections and SAT1–SAT2 intersections for an MLTAN offset of 2 hours. In that scenario, simulated SAT1–SAT2 revisits recur near the same latitude bands and at approximately the same Δt as self-intersections. Conversely, the remaining scenarios exhibit less agreement between self-intersections and SAT1–SAT2 intersections, suggesting that greater (smaller) differences in equatorial crossover times may give rise to more diverse (repetitive) resampling coverage.
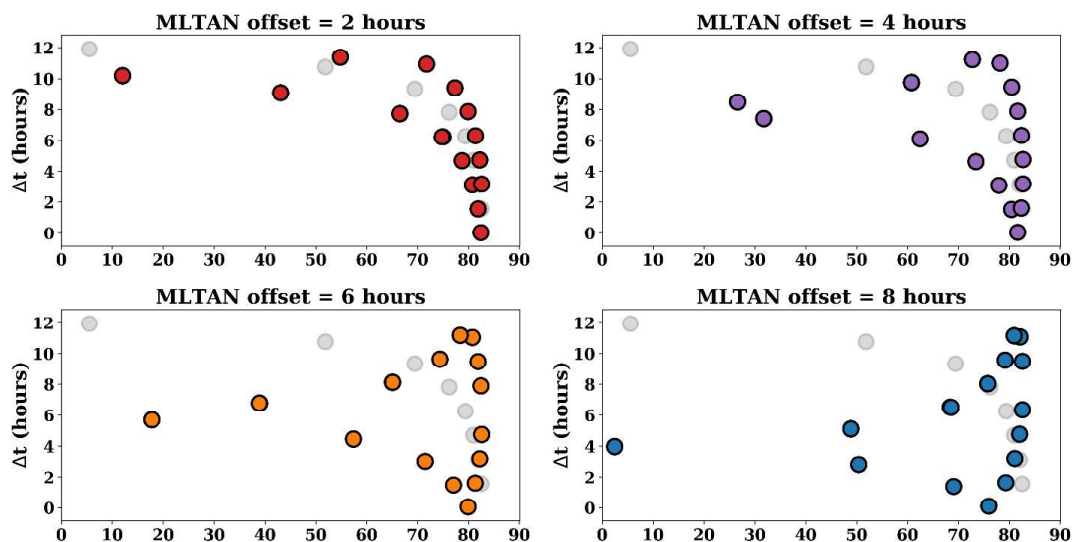
510 **Figure 17 shows time versus latitude for simulated SAT1–SAT2 intersections for each scenario (shown in color). Simulated self-intersections for a CubeSat at the same altitude (525 km) have been superimposed for reference.**

6. Conclusions

515 This study underscores the novel scientific applications of PREFIRE afforded by two CubeSats in orbits with distinct equatorial crossing times. Understanding the processes that influence polar energy balance will rely heavily on the frequent resampling the mission's CubeSats provide. By simulating representative orbits and approximating where and when their ground tracks intersect, we establish a preliminary record of plausible PREFIRE resampling or "intersections." Retrieving intersection centers by examining the distance between the fourth scenes of each CubeSat allows resampling

520 statistics to be quickly assessed. This informs more detailed processing to extract co-located pixels from intersection regions.

The procedures prescribed in this study therefore empower us to estimate mission resampling before launch and may help guide future CubeSat missions tasked with similar objectives.

PREFIRE resampling will take three forms: SAT1 self-intersections, SAT2 self-intersections and SAT1–SAT2 intersections. Assuming fidelity between simulated and achieved orbits, we can reasonably expect hundreds of intersections per day for each intersection type. Approximately one-quarter will constitute self-intersections for a single CubeSat, while SAT1–SAT2 intersections will account for the remaining half. These ratios are preserved when we restrict our sample of intersections to include only the polar subset. Taken together, we conclude that intersection frequency nearly quadruples with the addition of a second CubeSat, which alternatively suggests that about 75% of intersections will be lost in the event that one satellite becomes inoperable. Note that the number of self-intersections is nearly identical for both CubeSats, indicating that an altitude difference on the order of 10 km has little impact on self-intersection frequency.

The analysis further suggests that about three-quarters of both the self-intersections and SAT1–SAT2 intersections will occur at high latitudes, with the remaining quarter evenly split between low- and mid-latitude sectors. Self-intersections mutually coalesce in discrete, time-invariant latitude bands, forming eight bands in either hemisphere with latitudinal gaps in coverage. In addition, the elapsed time between self-intersection crossovers decreases monotonically as intersections move poleward, ranging from roughly 12 hours near the equator to the theoretical lower bound of 1.5 hours near the maximum sampling latitude.

By comparison, we expect to achieve much greater spatial and temporal coverage with intersections between CubeSats. As simulated, the PREFIRE CubeSats resample one another in a cyclic, time-varying fashion rather than in discrete latitude bands. SAT1–SAT2 intersections exhibit staggered modes that oscillate meridionally over time. Similarly, the elapsed time between SAT1–SAT2 intersections will not decrease monotonically with increasing latitude. Instead, resampling between CubeSats will oscillate between various time differences, sampling the greatest range of timescales near the maximum sampling latitude. While more than 75% of intersections occur poleward of 60°, the remaining intersections cover all latitudes, with the resulting distribution exhibiting a monotonic decrease in frequency approaching the equator. Unlike self-intersections, some intersections between satellites exhibit time differences less than a full orbit period. This includes a region between roughly 72° and 78° in either hemisphere where so-called "short-term revisits" occur. These short-term revisits are ideal candidates for monitoring the inter-calibration between CubeSats and will be used accordingly during the mission.

These results are based on the satellite altitudes used in the orbit simulations. The cyclic resampling observed in the simulations follows from the slightly different orbital periods of the satellites, providing excellent spatial and temporal coverage. This can be contrasted with the scenarios from Sect. 5, for which hypothetical CubeSat pairs were prescribed identical altitudes. In those simulations, SAT1–SAT2 intersections occurred in discrete latitude bands, similar (though not identical) to the coverage associated with self-intersections. Additionally, the spatio-temporal profile of intersections between CubeSats can be shown to vary based on the offset in their equatorial crossing times, with a smaller (greater) offset yielding SAT1–SAT2 intersections having more (less) coverage agreement with self-intersections. Together, these results

555 have strong implications concerning CubeSat utility in studying atmospheric processes, informing us that resampling may be optimized by staggering the altitudes of two or more CubeSats. They also inform us that the MLTAN combinations selected will affect resampling coverage between CubeSats. We note that, for any of the analyses undertaken here, SAT1—SAT2 intersections enhance the spatial and temporal coverage compared to self-intersections alone.

One appealing consequence of the short-term revisits formed by two satellites is the emergence of a technique for
560 inter-calibrating the two satellites. Monitoring intersections on timescales sufficiently small so as to ensure conditions remain virtually static between crossovers provides a means for rapidly identifying drifts in instrument performance. Initial differences in spectral radiances between the eight scenes of TIRS1 and the eight scenes of TIRS2 establish a baseline offset against which future differences can be compared. Drift in any scene on either TIRS may be identified when differences for that scene relative to the other TIRS deviate from the baseline. More generally, for homogeneous scenes, spectral radiances
565 for all "common pixels" of each intersection could be plotted and deviations from the resulting "partial" Planck functions would be indicative of drift in one of the scenes from the two sensors. Ultimately, operational inter-calibration will undoubtedly present greater challenges than those accounted for in this study. The fundamental premises described in this study will nonetheless help guide PREFIRE calibration and, we hope, future generations of CubeSat missions.

570 **APPENDIX A: TIRS channels**

TIRS1 channel centers (μm)	TIRS2 channel centers (μm)
2.95	4.20
3.80	5.05
4.64	5.89
5.48	6.73
8.02	9.27
8.86	10.11
9.70	10.95
10.55	11.80

11.39	12.64
12.24	13.48
13.08	14.33
15.61	16.86
16.45	17.70
17.30	18.55
18.14	19.39
18.99	20.24
19.83	21.08
20.67	21.92
21.52	22.77
22.36	23.61
23.20	24.45
24.05	25.30
24.89	26.14
25.74	26.99
26.58	27.83
27.42	28.67
28.27	29.52

30.80	32.05
31.64	32.89
32.49	33.74
33.33	34.58
34.17	35.42
35.02	36.27
35.86	37.11
36.71	37.96
37.55	38.80
38.39	39.64
39.24	40.49
40.08	41.33
40.92	42.17
41.77	43.02
42.61	43.86
43.46	44.71
44.30	45.55
45.14	46.39
45.99	47.24

46.83	48.08
47.68	48.92
48.52	49.77
49.36	50.61
50.21	51.46
51.05	52.30
51.89	53.14
52.74	53.99

Table A1 lists central wavelengths for each channel of the PREFIRE TIRS.

Code and data availability. The simulated orbits ("granules") and GEOS-IT data were created for mission pre-launch and remain part of the pre-launch development code base. The orbit intersection code and corresponding code to extract co-located pixels is also part of the pre-launch database and are available directly from the lead author.

Author contributions. TSL is the Principal Investigator of PREFIRE and conceptualized the study. TSL also provided PREFIRE-related expertise. NV formulated and tested the study methods and facilitated the orbit resampling analyses. All figures and tables were created by NV. TM created the simulated orbit files used in this study, provided interpolated GEOS-IT data, and contributed ongoing technical assistance.

Competing interests. The authors declare they have no conflict of interest.

References
Anheuser, J., Weisz, E., and Menzel, P. W.: Low earth orbit sounder retrieval products at geostationary earth orbit spatial and temporal scales, J. Appl. Remote Sens., 14, https://doi.org/10.1117/1.JRS.14.048502, 2020.

590   Bentley, J. L.: Multidimensional binary search trees used for associative searching. Communications of the ACM, 18, 509–517, doi:10.1145/361002.361007, 1975.

Blackwell, W. J., Braun, S., Bennartz, R., Velden, C., DeMaria, M., Atlas, R., Dunion, J., Marks, F., Rogers, R., Annane, B., and Leslie, R. V.: An overview of the TROPICS NASA Earth venture mission, Quart. J. Roy. Meteorological Soc., 144, 16-26, https://doi.org/10.1002/qj.3290, 2018.

595   Cao, C., and Heidinger, A. K.: Inter-comparison of the longwave infrared channels of MODIS and AVHRR/NOAA-16 using simultaneous nadir observations at orbit intersections, Proc. SPIE Int. Symp. on Opt. Sci. Technol., Vol. 4814, Earth Observing Systems VII, 2002, Seattle, WA, SPIE, doi:10.1117/12.451690, 2002.

Cao, C., M. Weinreb, and Xu, H.: Predicting Simultaneous Nadir Overpasses among Polar-Orbiting Meteorological Satellites for the Intersatellite Calibration of Radiometers. J. Atmos. Oceanic Technol., 21, 537-542,
600   https://doi.org/10.1175/1520-0426(2004)021<0537:PSNOAP>2.0.CO;2, 2004.

Cao, C., Weng, F., Goldberg, M., Wu, X., Xu, H., and Ciren, P.: Intersatellite Calibration of Polar-orbiting Radiometers using the SNO/SCO Method, 2005 IEEE International Geoscience and Remote Sensing Symposium, 1, doi: 10.1109/IGARSS.2005.1526116, 2005.

Chander, G., Hewison, T. J., Fox, N., Wu, X., Xiong, X., and Blackwell, W. J.: Overview of Intercalibration of Satellite
605   Instruments, IEEE Trans. Geos. and Remote Sens., 51, 1056-1080, doi:10.1109/TGRS.2012.2228654, 2013.

Chen, X., Huang, X., and Flanner, M. G.: Sensitivity of modeled far-IR radiation budgets in polar continents to treatments of snow surface and ice cloud radiative properties, Geophys. Res. Lett., 41, 6530-6537, doi:10.1002/2014GL0612160, 2014.

Drouin, B. J., Kahn, B., Lim, B., Merrelli, A., Nelson, E., Quinn, G., Nagle, F., and L'Ecuyer, T.: Orbital Trade Study for the PREFIRE Mission, 2022 IEEE Aerospace Conference, Big Sky, MT, USA, 1-7, doi: 10.1109/AERO53065.2022.9843312,
610   2022.

Feldman, D. R., Collins, W. D., Pincus, R., Huang, X., and Chen, X.: Far-infrared surface emissivity and climate, Proceedings of the National Academy of Sciences, 111, 16297-16302. https://doi.org/10.1073/pnas.1413640111, 2014.

Freidman, J. H., Bentley, J. L., and Finkel, R. A.: An Algorithm for Finding Best Matches in Logarithmic Expected Time, ACM Transactions on Mathematical Software, 3, 209–226, doi:10.1145/355744.355745, 1977.

615   Hanel, R. A., Conrath, B. J., Kunde, V. G., Prabhakara, C., Revah, I., Salomonson, V. V., and Wolford, G.: The Nimbus 4 infrared spectroscopy experiment: 1. Calibrated thermal emission spectra, J. Geophys. Res., 77, 2629-2641, doi:10.1029/JC077i015p02629, 1972.

Harries, J., Carli, B., Rizzi, R., Serio, C., Mlynczak, M., Palchetti, L., Maestri, T., Brindley, H., and Masiello, G.: The far-infrared Earth, Rev. Geophys., 46, RG4004, doi:10.1029/2007RG000233, 2008.

620   Heidinger, A. K., Cao, C., and Sullivan, J. T.: Using Moderate Resolution Imaging Spectrometer (MODIS)to calibrate advanced very high resolution radiometer reflectance channels, J. Geophys. Res.,107, 4702, doi:10.1029/2001JD002035, 2002.

Huang, X., Chen, X., Potter, G. L., Orepoulos, L., Cole, J. N. S., Lee, D., and Loeb, N. G.: A Global Climatology of Outgoing Longwave Spectral Cloud Radiative Effect and Associated Effective Cloud Properties, J. Climate, 27, 7475-7492,

625   https://doi.org/10.1175/JCLI-D-13-00663.1, 2014.

Huang, X., Chen, X., Zhou, D. K., and Liu, X.: An Observationally Based Global Band-by-Band Surface Emissivity Dataset for Climate and Weather Simulations, J. Atmos. Sci., 73, 3541-3555, https://doi.org/10.1175/JAS-D-15-0355.1, 2016.

Iacovazzi, Jr., R. and Cao, C.: Reducing Uncertainties of SNO-Estimated Intersatellite AMSU-A Brightness Temperature Biases for Surface-Sensitive Channels, J. Atmos., and Oceanic Tech., 25, 1048-1054, DOI:

630   https://doi.org/10.1175/2007JTECHA1020.1, 2008.

Kempe, V., Oertel, D., Schuster, R., Becker-Ross, H., and Jahn, H.: Absolute IR-spectra from the measurement of Fourier-spectrometers aboard Meteor 25 and 28, 7, 1403-1416, https://doi.org/10.1016/0096-5765(80)90015-6, 1980.

L'Ecuyer, T. S., Drouin, B. J., Anheuser, A., Grames, M., Henderson, D. S., Huang, X., Kahn, B. H., Kay, J. E., Lim, B. H., Mateling, M., Merrelli, A., Miller, N. B., Padmanabhan, S., Peterson, C., Schlegel, N.-J., White, M. L., and Xie, Y.: The

635   Polar Radiant Energy in the Far Infrared Experiment: A New Perspective on Polar Longwave Energy Exchanges, Bull. Amer. Meteor. Soc., 102, E1431-E1449, https://doi.org/10.1175/BAMS-D-20-0155.1, 2021.

Miller, N. B., Merrelli, A., L'Ecuyer, T. S., and Drouin, B. J.: Simulated Clear-Sky Water Vapor and Temperature Retrievals from PREFIRE Measurements, J. Atmos. Oceanic Technol., 40, 645-659, https://doi.org/10.1175/jtech-d-22-0128.1, 2023.

Nagle, F. W., and Holz, R. E.: Computationally Efficient Methods of Collocating Satellite, Aircraft, and Ground

640   Observations, J. Atmos. Oceanic Technol., 26, 1585-1595, https://doi.org/10.1175/2008JTECHA1189.1

Palchetti, L., Brindley, H., Bantges, R., Buehler, S. A., Camy-Peyret, C., Carli, B., Cortesi U., Del Bianco, S., Di Natale, G., Dinelli, B. M., Feldman, D., Huang, X. L., Labonnote, L. C., Libois, Q., Maestri, T., Mlynczak, M. G., Murray, J. E., Oetjen, H., Ridolfi, M., Riese, M., Russell, J., Saunders, R., and Serio, C.: FORUM: Unique far-infrared satellite observations to better understand how earth radiates energy to space, Bull. Amer. Meteor. Soc.,101, E2030–E2046.

645   https://doi.org/10.1175/bams-d-19-0322.1, 2020.

Rees, W. G.: Orbital subcycles for Earth remote sensing satellites, International Journal of Remote Sensing, 13, 825-933, doi:10.1080/01431169208904156, 1992.

Rew, R. K., and Davis, G. P.: NetCDF: An Interface for Scientific Data Access, IEEE Computer Graphics and Applications, 10, 76-82, 1990.

650   Stephens, G., Freeman, A., Richard, E., Pilewskie, P., Larkin, P., Chew, C., Tanelli, S., Brown, S., Posselt, D., and Peral, E.: The Emerging Technological Revolution in Earth Observations, Bull. Amer. Meteor. Soc., 101, E274–E285, https://doi.org/10.1175/BAMS-D-19-0146.1, 2020.

Tobin, D. C., Revercomb, H. E., Moeller, C. C., and Pagano, T. S.: Use of Atmospheric Infrared Sounder high–spectral resolution spectra to assess the calibration of Moderate resolution Imaging Spectroradiometer on EOS Aqua, J. Geophys.

655   Res., 111, D09S05, doi:10.1029/2005JD006095, 2006.

Wang, L., Cao, C., and Ciren, P.: Assessing NOAA-16 HIRS radiance accuracy using simultaneous nadir overpass observations from AIRS, J. Atmos. Ocean. Technol, 24, 1546–1561, https://doi.org/10.1175/JTECH2073.1, 2007.

Weisz, E., and Menzel, P. W.: Imager and sounder data fusion to generate sounder retrieval products at an improved spatial and temporal resolution, J. Appl. Remote Sens., 13, https://doi.org/10.1117/1.JRS.13.034506, 2019.

660